Spontaneous nanometric magnetic bubbles with various topologies in spin-reoriented $La_{1-x}Sr_xMnO_3$

Licong Peng, Ying Zhang, Deshun Hong, Bo Zhang, Jianqi Li, Jianwang Cai, Shouguo Wang, Jirong Sun, and Baogen Shen

Citation: Appl. Phys. Lett. **113**, 142408 (2018); doi: 10.1063/1.5051014
View online: https://doi.org/10.1063/1.5051014
View Table of Contents: http://aip.scitation.org/toc/apl/113/14
Published by the American Institute of Physics

Spontaneous nanometric magnetic bubbles with various topologies in spin-reoriented $La_{1-x}Sr_xMnO_3$

Licong Peng,[1,2] Ying Zhang,[1,a)] Deshun Hong,[1,2] Bo Zhang,[1,2] Jianqi Li,[1,2] Jianwang Cai,[1,2] Shouguo Wang,[3] Jirong Sun,[1,2] and Baogen Shen[1,2]

[1]*Beijing National Laboratory for Condensed Matter Physics, Institute of Physics, Chinese Academy of Sciences, Beijing 100190, China*

[2]*School of Physical Sciences, University of Chinese Academy of Sciences, Beijing 100049, China*

[3]*School of Materials Science and Engineering, University of Science and Technology Beijing, Beijing 100083, China*

(Received 5 August 2018; accepted 20 September 2018; published online 5 October 2018)

Topological zero-field nanometric domains and their capability to be manipulated by external fields show potential applications in spintronics. Here, the spontaneous magnetic bubbles (≈100 nm in diameter) are observed at zero field in a ferromagnetic manganite $La_{1-x}Sr_xMnO_3$ ($0.15 < x < 0.2$) by using Lorentz transmission electron microscopy. The spin reorientation as a function of temperature drives the magnetic domain transition from traditional 180° in-plane domains to helical stripes and bubbles, resulting in rich magnetic configurations with various topologies. It directly demonstrates that the dynamic motion of Bloch lines in bubbles introduces the topologic transition under the application of magnetic fields. *Published by AIP Publishing.*

https://doi.org/10.1063/1.5051014

Recently, the promising results from nanometric topological skyrmions, especially the discovery of their electric-current manipulation behaviors, have broadened the skyrmion material exploration from metals[1] to insulators,[2] from ferromagnets[1,2] to antiferromagnets,[3] and from bulk[1,2,4] to multilayers.[5–7] Many kinds of spin configurations in topological domains including chiral skyrmions, biskyrmions, antiskyrmions have been recognized.[1,8–11] The typical chiral skyrmions present a circle-like swirling pattern with single helicity, and biskyrmions show opposite swirling of spin helicities.[9–11] Antiskyrmions reveal both helicoid and cycloid spin propagations, showing two bright and two dark lobes in a Lorentz transmission electron microscopy (L-TEM) image.[8] It is recently considered that magnetic bubbles with a winding number $S = 1$ are topologically equivalent to skyrmions.[4,12] Magnetic bubbles are in the form of cylindrical domains with narrow domain walls separating the out-of-plane magnetization into antiparallel and parallel magnetization regions related to the external field H_z.[12,13] The magnetizations gradually rotate within the domain wall region and by which, the two degrees of freedom, i.e., helicity and vorticity are defined. The helicity is the rotational direction of in-plane magnetizations along the perimeter, and the vorticity is represented by a winding number $S = \frac{\int_0^{2\pi} d\varnothing(\varphi)}{2\pi}$,[13] characterizing the topology of magnetic bubbles. Being distinct from the relatively fixed spin configuration of the skyrmions, the bubble configuration can have different topological numbers (2, 1, or 0) and can be easily tuned via dynamic motion of Bloch lines (BLs).[14,15]

The size of traditional magnetic bubbles in uniaxial ferromagnets[16] and garnet films[17] with perpendicular anisotropy usually ranges from several hundred nanometers to micrometers.[18] These large magnetic bubbles were intensively studied since the 1970s and were further applied in memory devices.[19,20] Theoretical[21] and experimental studies[16,17] indicate that the ratio of the magnetic anisotropy and magnetostatic energies, so-called quality factor $Q = 2K_u/\mu_0 M_s^2$ (μ_0 is the vacuum permeability, and M_s and K_u present the saturation magnetization and the uniaxial anisotropy coefficient), are critical parameters to determine the generation and the size of the magnetic bubbles. Magnetic bubbles have been found in a high-Q system, i.e., when $Q > 1$,[17] and in some materials with $Q \sim 1$, such as in hexaferrites,[16] MnNiGa,[22] and Pt/Co/Ta multilayers.[23,24] Doped transition-metal oxides like manganite systems are well known for their rich physical properties and magnetic phase transitions due to the combination of coupling between charge, spin, orbital, and broad degrees of freedom.[9,25–27] Biskyrmions have been found in $La_{2-2x}Sr_{1+2x}Mn_2O_7$ ($x = 0.315$)[9] and spontaneous bubbles by doping different amounts of Ru are reported in $La_{1.2}Sr_{1.8}(Mn_{1-y}Ru_y)_2O_7$.[27] Usually, the stripe domain instead of a bubble domain is the ground state due to the minimization of the sum of the domain wall energy and the magnetostatic energy. If the nanometric magnetic bubbles can be realized at zero field, the engineering difficulty and energy consumption would be reduced, conveniently prompting its nonvolatile memory device applications.[28] Furthermore, by taking advantage of the various topologies in magnetic bubbles,[13,18] the manipulation of the topological spin textures could be applied in the spintronic devices.

Here, the generation of spontaneous nanometric bubbles (∼100 nm) at zero field and the dynamic changes of topological spin textures as a function of temperatures or magnetic fields are investigated by means of L-TEM in $La_{1-x}Sr_xMnO_3$ ($0.15 < x < 0.2$). The temperature-driven spin reorientation transition introduces the ferromagnetic (FM) structure change from 180° in-plane domains into spontaneous bubbles with variations of topology.

a)Email: zhangy@iphy.ac.cn

A polycrystalline bulk sample of $La_{1-x}Sr_xMnO_3$ (LSMO) ($0.15 < x < 0.2$) was synthesized by a conventional solid-state reaction. The starting materials, La_2O_3, $SrCO_3$, and MnO_2, were mixed with the nominal ratio and calcined in air at 1000 °C and 1350 °C with intermediate grinding. The phase purity of the bulk sample was confirmed by X-ray diffraction, and the magnetic properties were measured using a superconducting quantum interference magnetometer-vibrating sample magnetometer (SQUID-VSM). A thin plate was cut from the bulk sample and thinned by mechanical polishing and ion-beam milling using a Gatan precision ion polishing system (PIPS) operated with an acceleration voltage of 4 kV at room temperature. The inversion contrasts of magnetic domains were investigated by using *in situ* L-TEM (JEOL 2100F) with a liquid-nitrogen cooling specimen holder. The magnetic field perpendicular to the thin sample is applied via adjusting objective lens current. The in-plane magnetization textures of magnetic domains were obtained by a phase retrieval technique based on the transport of intensity equation (TIE).[29]

The temperature dependence of the magnetic domain evolution is presented in the under-focused L-TEM images [Figs. 1(a)–1(e)]. The selected-area electron diffraction (SAED) pattern shows that the observed grains are along the [110] zone axis [Fig. 1(f)]. The temperature dependence of the magnetic moment curve (M-T) and its derivative [Fig. 1(g)] demonstrate the ferromagnetic transition temperature T_C about 238 K and a spin reorientation transition peak approximately at 125 K. The spin reorientation transition results in the magnetic domain change from 180° in-plane to helical domains, which is elaborated in Figs. 1(a)–1(e) by real-space L-TEM observation. At room temperature, no magnetic contrast is observed in the paramagnetic state [Fig. 1(a)]. When the temperature drops just lower than T_C, very weak magnetic contrast develops at the edge of the thin plate at 227 K (not shown here), indicating the gradual increase in the magnetization amplitude over the thermal disturbance. Typical 180° ferromagnetic domains with the in-plane magnetization in the width about 1 μm are observed at 194 K in Fig. 1(b). The corresponding magnetic spin configuration and M_y profile are schematically described in Fig. 1(h). The collapse of large 180° domains into irregular small domains at 184 K [Fig. 1(c)] and 173 K [Fig. 1(d)] is demonstrated. The spontaneous mixed state of helical stripes and bubble domains is observed near the spin reorientation transition temperature about 123 K [Fig. 1(e)]. The spin reorientation transition is considered to play a critical role in the generation of the topological spin configuration.[23,24] The corresponding helical magnetic spin configuration and sine-like M_y profile are schematically described in Fig. 1(i). Therefore, the essential nature of zero-field bubble generation in correlation with the spin reorientation transition is clearly elaborated in these real space L-TEM images.

The magnetic-fields dependence of the spontaneous magnetic domain textures is observed as shown in Fig. 2. The size distribution for zero-field bubbles in Fig. 2(a) is analyzed to be around 70–140 nm [Fig. 2(g)], which is far below the size of traditional bubbles and more close to skyrmion size, thus promising for the application of the high-density storage device. Based on the mixed stripes and bubbles in Fig. 2(a), the dynamic evolution behaviors are investigated via *in-situ* L-TEM while altering the external magnetic fields. The curved stripes appear to be pinched off and generate irregular bubbles when the field is above 0.23 T [Fig. 2(b)]. The bubble size turns to shrink at the magnetic field exceeding 0.44 T [Fig. 2(c)] and completely disappears into the saturated ferromagnetic state above 0.7 T [Fig. 2(d)]. The area of stripes and bubbles is separately measured

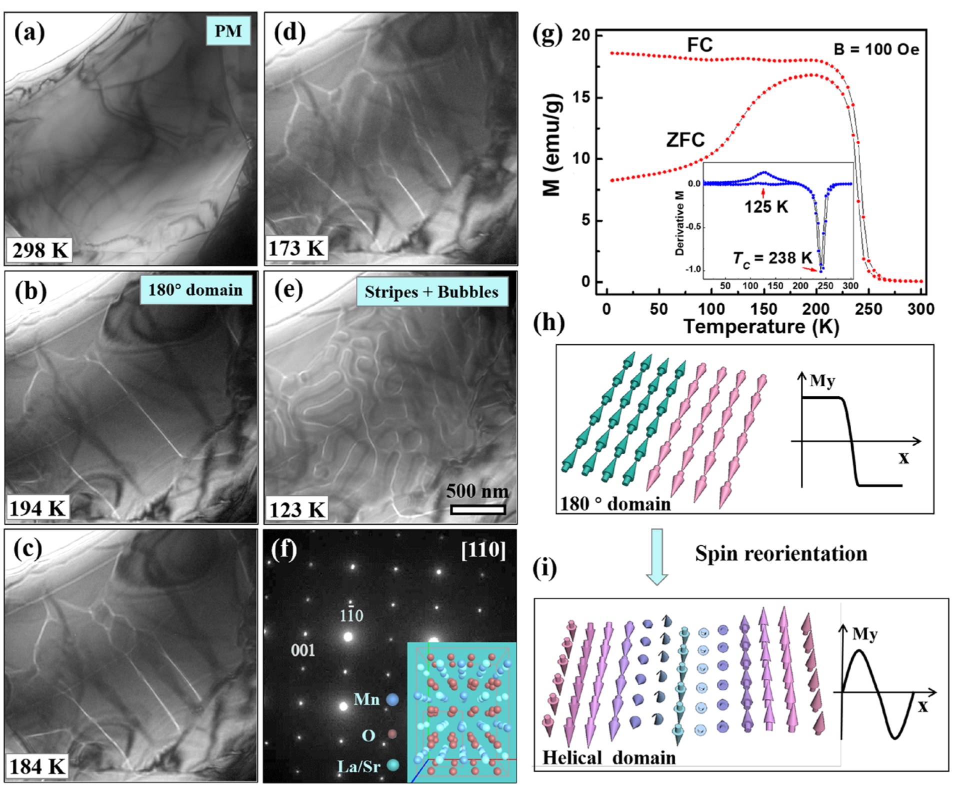

FIG. 1. Temperature dependence of the spontaneous magnetic domain evolution in under-focused L-TEM images at zero field: (a) 298 K, (b) 194 K, (c) 184 K, (d) 173 K, and (e) 123 K. Diffraction pattern (f) showing the grain observation along the [110] zone axis. (g) The magnetic moment curve and its derivative as a function of temperature showing a ferromagnetic phase transition at 238 K and a spin reorientation transition near 125 K. (h) Schematic spin configuration for 180° domains and (i) helical stripes with the corresponding transverse component M_y line profiles along the x axis. The scale bar in (e) corresponds to 500 nm.

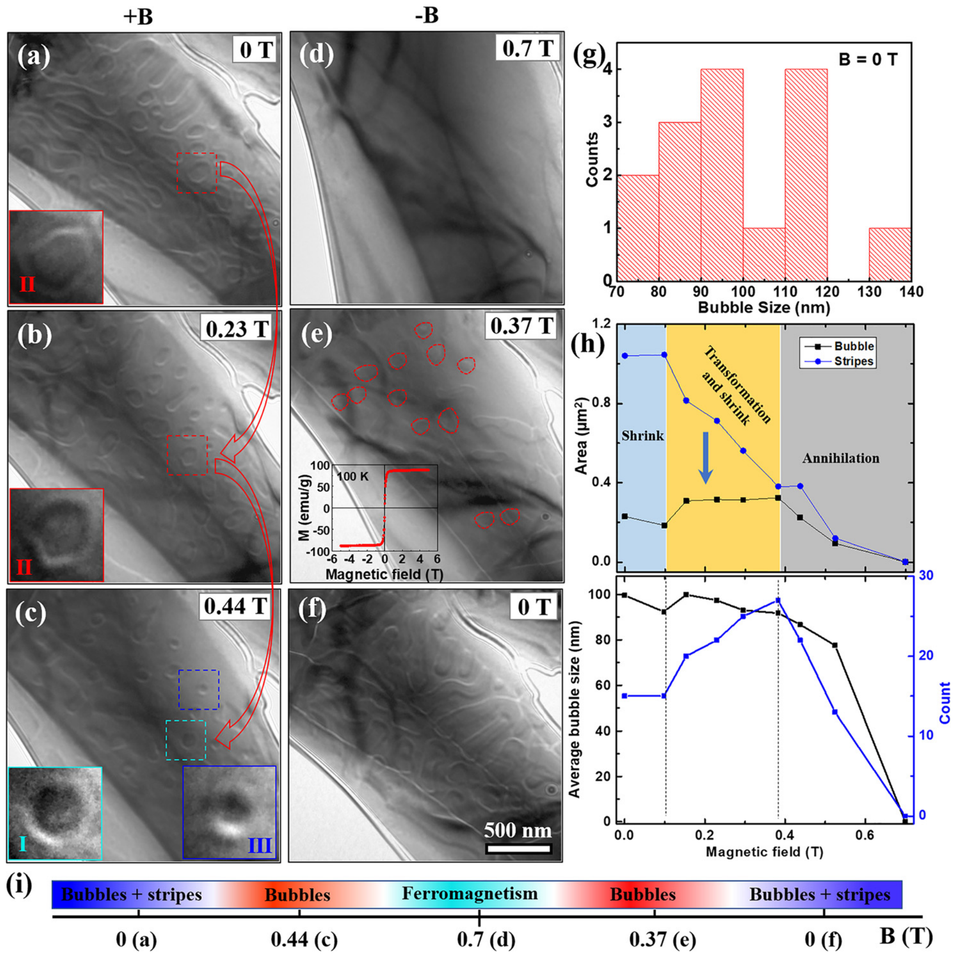

FIG. 2. Magnetic fields dependence of magnetic domain evolution in L-TEM images at 100 K. (a)–(c) The stripes transforming into bubbles with the topology change while increasing the magnetic fields. The insets to (a)–(c) show the enlarged view of various topologies of bubbles. (d)–(f) The generation of bubbles and stripes while decreasing the magnetic fields from 0.7 T to 0 T. The inset of (e) shows the M-H curve at 100 K. (g) Size distribution of spontaneous bubbles in (a). (h) The area ratio of the stripes and bubbles (up) and the distribution of averaged bubbles size and number (bottom) with the increasing magnetic fields. (i) The schematic illustration of the reversible magnetic domain revolution with changing the external magnetic fields. The scale bar in (f) corresponds to 500 nm.

during the evolution at different magnetic fields as shown in Fig. 2(h). The blue region identified from the decreased area and the unchanged bubble numbers with the smaller size demonstrate the size shrinking behavior of bubbles and stripes for the magnetic field of 0–0.1 T. In the magnetic field range from 0.1 T to 0.38 T, the stripes start to transform into bubbles and the initial zero-field bubbles keep shrinking, which is summarized as the decreased stripe area and the increased bubble numbers. Further increasing the magnetic fields from 0.38 T to 0.7 T, the annihilation into the saturated ferromagnetic state is dominated with both the area and numbers of stripes and bubbles sharply dropping to zero. Gradually reducing the external magnetic field from this FM state [Fig. 2(d)], the bubbles reappear first [Fig. 2(e)] and then the mixed bubbles and stripes are obtained at zero field [Fig. 2(f)]. The nearly reversible magnetic domain evolution with the increasing/decreasing magnetic fields is summarized in Fig. 2(i), which is related to the small hysteresis as indicated by the M-H curve [inset of Fig. 2(e)].

The BLs in the bubble domain wall are very sensitive to the stimuli of magnetic fields,[13,14] therefore introducing susceptible topological transition of magnetic bubbles via BL motion [the insets of Figs. 2(a)–2(c)]. A pair of BLs in the domain wall of a zero-field bubble is observed to move along the circle domain wall and finally annihilate when increasing the magnetic fields. To further characterize the topological spin textures of the bubble transition [numbered in Figs. 2(a)–2(c)], the magnetization distribution is analyzed from the magnified under- and over-focused L-TEM images using the TIE method (Fig. 3). The initial bubble at zero field accompanied by a pair of Bloch lines (marked with arrows) belongs to the type II bubble with a winding number $S = 0$ [Figs. 3(a)–3(d)]. The spatial position of BLs changes with the external magnetic fields, but the winding number remains 0 when the magnetic field is not high enough [Figs. 3(e)–3(h)]. Further increasing the magnetic fields above 0.44 T, the BLs annihilate and type I bubble with a unity winding number $S = 1$ appear [Figs. 3(i)–3(l)]. The magnetic helicity with counter-clockwise rotation of magnetic moments is considered topologically equal to skyrmions.[4] The transition from type II to type I bubble via real-space observation clearly demonstrates the topological transitions driven by the external magnetic field. During the entire process, another topological texture with opposite helicity indicates the winding number $S = 2$ in Figs. 3(m)–3(p). The variation of magnetic bubbles under the excitation of magnetic fields is related to the topological protection stability for the bubbles with different topological numbers. Bubbles with the topological zero number should be easily affected by external fields in comparison with those with the nonzero topological number.

The dynamic phase transition between topological bubbles and ferromagnetic state is determined by the corresponding energy barrier[30–32] and is schematically illustrated in Fig. 4(c), where E_0 is the condition at which the two states are energetically degenerate. The obtained energetically

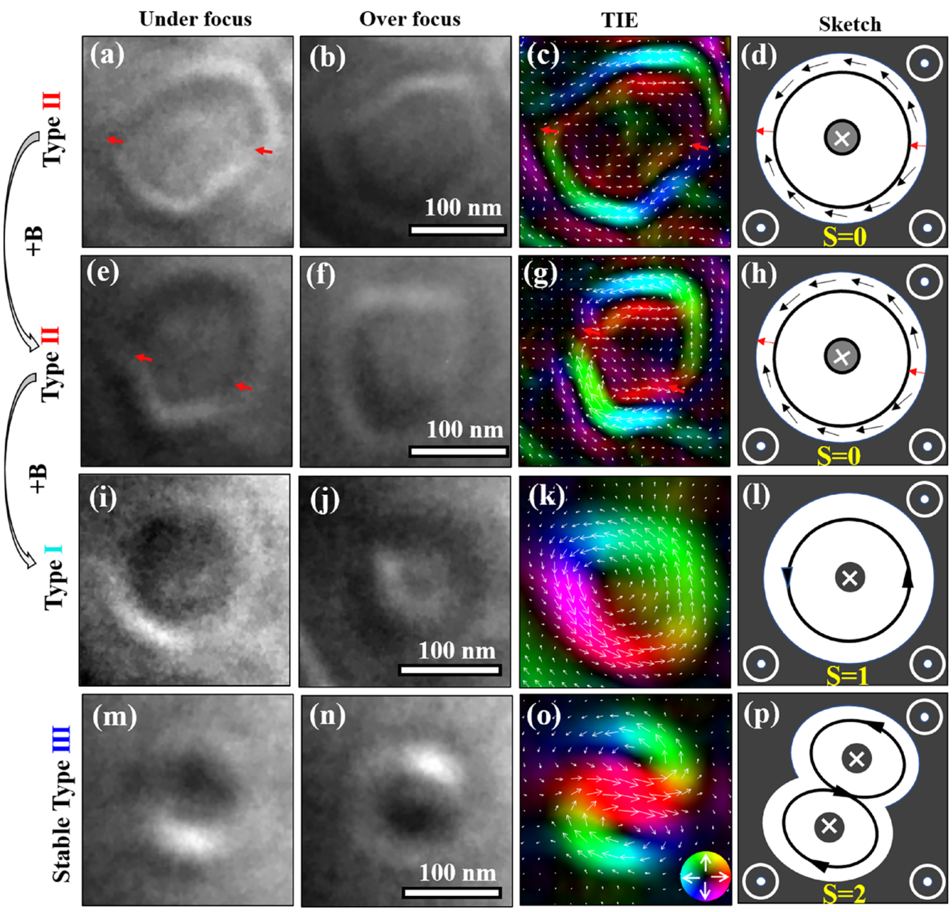

FIG. 3. The configuration of magnetic bubbles with varieties of topologies. Under-focused and over-focused L-TEM images of bubbles and corresponding magnetization textures (a)–(d) Type II bubble at zero field. (e)–(h) Distorted type II bubble while increasing the magnetic fields. (i)–(l) Type I bubble induced from type II. (m)–(p) Type III bubble. Colors and white arrows display the direction and magnitude of in-plane magnetizations, while dark color indicates the magnetizations almost along the out-of-plane direction. The direction of the external field pointing out of paper (marked with white dot) antiparallel to the magnetization inside the core (marked with black cross).

lower state (topological bubbles or FM state) can be tailored by the energy competition.[30,31] For example, the reversible transition between bubbles and the FM state is easier to be obtained by varying the magnetic fields near B_0 as experimentally identified in Figs. 2(a)–2(f). Furthermore, a phenomenological free-energy model[31] is used to quantitatively evaluate the energy barrier between bubbles and ferromagnetic (FM) transition. In order to obtain reliable statistic data, the L-TEM image with the distribution of complete bubbles is divided into 4 equal areas. The calculated energy barrier at the condition of 100 K and 0.44 T is about 6.36×10^{-16} J which is an order of magnitude larger than the value of 1.4×10^{-17} J in $La_{0.5}Ba_{0.5}MnO_3$ at $\sim$360 K.[32] The higher energy barrier in our study could be due to the lower temperature.

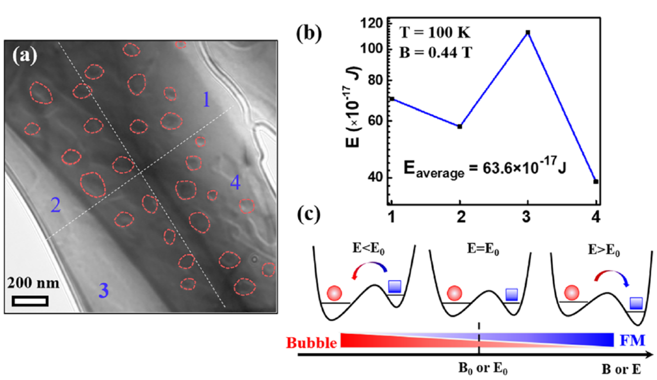

FIG. 4. Approximate calculation of the energy barrier between the complete bubble state and the ferromagnetic state at 0.44 T and 100 K. (a) L-TEM image of magnetic bubble distribution. (b) The quantitative energy barrier calculation from the four parts in (a) based on the phenomenological free-energy model. (c) Sketch of the potential energy between the two states; E_0 is the energetically degenerated state.

In summary, the generation of zero-field nanometric magnetic bubbles with various topological structures under external fields is demonstrated via *in-situ* real-space L-TEM imaging in LSMO. The temperature-driven spin reorientation transition contributes the domain configuration evolution from conventional in-plane to helical magnetization, resulting in the spontaneous bubble domains at zero field. The dynamic motion of BLs and the topological transition driven by the perpendicular field are directly demonstrated. In addition, the energy barrier between bubbles and ferromagnetic (FM) transition is approximately extracted by using the phenomenological free-energy model. The zero-field bubbles and the field-driven topology change in manganite oxides provide great insights into the manipulation of topological spin textures in the field of spintronics.

This work was supported by the National Key Research and Development Program of China (Grant No. 2016YFB0700902), National Natural Science Foundation of China (Grant Nos. 51590880, 51431009, 51561145003, and 51625101), and Youth Innovation Promotion Association, CAS, No. 2015004.

[1] X. Z. Yu, N. Kanazawa, Y. Onose, K. Kimoto, W. Z. Zhang, S. Ishiwata, Y. Matsui, and Y. Tokura, Nat. Mater. **10**, 106 (2011).
[2] S. Seki, X. Z. Yu, S. Ishiwata, and Y. Tokura, Science **336**, 198 (2012).

[3]G. Yu, A. Jenkins, X. Ma, S. A. Razavi, C. He, G. Yin, Q. Shao, Q. L. He, H. Wu, W. Li, W. Jiang, X. Han, X. Li, A. C. Bleszynski Jayich, P. K. Amiri, and K. L. Wang, Nano Lett. **18**, 980 (2018).
[4]N. Nagaosa and Y. Tokura, Nat. Nanotechnol. **8**, 899 (2013).
[5]A. Fert, N. Reyren, and V. Cros, Nat. Rev. Mater. **2**, 17031 (2017).
[6]W. J. Jiang, P. Upadhyaya, W. Zhang, G. Q. Yu, M. B. Jungfleisch, F. Y. Fradin, J. E. Pearson, Y. Tserkovnyak, K. L. Wang, and O. Heinonen, Science **349**, 283 (2015).
[7]W. Jiang, X. Zhang, G. Yu, W. Zhang, X. Wang, M. Benjamin Jungfleisch, J. E. Pearson, X. Cheng, O. Heinonen, K. L. Wang, Y. Zhou, A. Hoffmann, and S. G. E. Te Velthuis, Nat. Phys. **13**, 162 (2017).
[8]A. K. Nayak, V. Kumar, T. Ma, P. Werner, E. Pippel, R. Sahoo, F. Damay, U. K. Rößler, C. Felser, and S. P. Parkin, Nature **548**, 561 (2017).
[9]X. Z. Yu, Y. Tokunaga, Y. Kaneko, W. Z. Zhang, K. Kimoto, Y. Matsui, Y. Taguchi, and Y. Tokura, Nat. Commun. **5**, 3198 (2014).
[10]W. Wang, Y. Zhang, G. Xu, L. Peng, B. Ding, Y. Wang, Z. Hou, X. Zhang, X. Li, E. Liu, S. Wang, J. Cai, F. Wang, J. Li, F. Hu, G. Wu, B. Shen, and X. X. Zhang, Adv. Mater. **28**, 6887 (2016).
[11]L. Peng, Y. Zhang, M. He, B. Ding, W. Wang, J. Li, J. Cai, S. Wang, G. Wu, and B. Shen, J. Phys.: Condens. Matter **30**, 065803 (2018).
[12]X. Z. Yu, K. Shibata, W. Koshibae, Y. Tokunaga, Y. Kaneko, T. Nagai, K. Kimoto, Y. Taguchi, N. Nagaosa, and Y. Tokura, Phys. Rev. B **93**, 134417 (2016).
[13]X. Yu, Y. Tokunaga, Y. Taguchi, and Y. Tokura, Adv. Mater. **29**, 1603958 (2017).
[14]A. P. Malozemoff and J. C. Slonczewski, *Magnetic Domain Walls in Bubble Materials* (Academic Press, 1979).
[15]R. S. Alex Hubert, *Magnetic Domains* (Springer, 2009).
[16]P. J. Grundy and S. R. Herd, Phys. Status Solidi **20**, 295 (1973).
[17]Y. S. Lin, P. J. Grundy, and E. A. Giess, Appl. Phys. Lett. **23**, 485 (1973).
[18]X. Yu, M. Mostovoy, Y. Tokunaga, W. Zhang, K. Kimoto, Y. Matsui, Y. Kaneko, N. Nagaosa, and Y. Tokura, Proc. Natl. Acad. Sci. **109**, 8856 (2012).
[19]M. Yamanouchi, D. Chiba, F. Matsukura, and H. Ohno, Nature **428**, 539 (2004).
[20]S. S. P. Parkin, M. Hayashi, and L. Thomas, Science **320**, 190 (2008).
[21]T. Garel and S. Doniach, Phys. Rev. B **26**, 325 (1982).
[22]S. L. Zuo, Y. Zhang, L. C. Peng, X. Zhao, R. Li, H. Li, J. F. Xiong, M. He, T. Y. Zhao, J. R. Sun, F. X. Hu, and B. G. Shen, Nanoscale **10**, 2260 (2018).
[23]M. He, G. Li, Z. Zhu, Y. Zhang, L. Peng, R. Li, J. Li, H. Wei, T. Zhao, X.-G. Zhang, S. Wang, S.-Z. Lin, L. Gu, G. Yu, J. Cai, and B. Shen, Phys. Rev. B **97**, 174419 (2018).
[24]M. He, L. Peng, Z. Zhu, G. Li, J. Cai, J. Li, H. Wei, L. Gu, S. Wang, T. Zhao, B. Shen, and Y. Zhang, Appl. Phys. Lett **111**, 202403 (2017).
[25]W. Jiang, X. Zhou, and G. Williams, Phys. Rev. Lett. **99**, 177203 (2007).
[26]W. Jiang, X. Zhou, and G. Williams, Phys. Rev. B **77**, 064424 (2008).
[27]D. Morikawa, X. Z. Yu, Y. Kaneko, Y. Tokunaga, T. Nagai, K. Kimoto, T. Arima, and Y. Tokura, Appl. Phys. Lett. **107**, 212401 (2015).
[28]T. Fukumura, H. Sugawara, T. Hasegawa, K. Tanaka, H. Sakaki, T. Kimura, and Y. Tokura, Science **284**, 1969 (1999).
[29]K. Ishizuka and B. Allman, J. Electron Microsc. (Tokyo) **54**, 191 (2005).
[30]N. Romming, C. Hanneken, M. Menzel, J. E. Bickel, B. Wolter, K. Von Bergmann, A. Kubetzka, and R. Wiesendanger, Science **341**, 636 (2013).
[31]L. Peng, Y. Zhang, W. Wang, M. He, L. Li, B. Ding, J. Li, Y. Sun, X.-G. Zhang, J. Cai, S. Wang, G. Wu, and B. Shen, Nano Lett. **17**, 7075 (2017).
[32]M. Nagao, Y.-G. So, H. Yoshida, M. Isobe, T. Hara, K. Ishizuka, and K. Kimoto, Nat. Nanotechnol. **8**, 325 (2013).